ACS SENSORS

pubs.acs.org/acssensors

Article

Photoelectrochemical Biosensor for DNA Formylation Detection in Genomic DNA of Maize Seedlings Based on Black Tio_2-Enhanced Photoactivity of MoS_2/WS_2 Heterojunction

Fei Li, Siyu Wang, Huanshun Yin,* Yan Chen, Yunlei Zhou, Jing Huang, and Shiyun Ai

Cite This: *ACS Sens.* 2020, 5, 1092−1101

Read Online

ACCESS | Metrics & More | Article Recommendations | Supporting Information

ABSTRACT: 5-Formylcytosine (5fC) is a rare base found in mammalian DNA, which is thought to be involved in the demethylation of DNA. As a stable epigenetic modification, 5fC participates in gene regulation and cell differentiation, and plays an important role in the growth and development of plants. However, the abundance of 5fC is only as low as 0.002−0.02% of cytosine. Therefore, to further understand the functions of 5fC, a rapid, highly sensitive, and efficient method is needed for detecting 5fC. Herein, a novel photoelectrochemical (PEC) biosensor was constructed for 5fC detection, where a MoS_2/WS_2 nanosheet heterojunction was employed as a photoactive material, amino-functionalized Fe_3O_4 and SMCC were used as a linker, 4-amino-3-hydrazino-5-mercapto-1,2,4-triazole was adopted as 5fC recognition reagent, and black TiO_2 (B-TiO_2) was used as a signal amplification unit. Under the optimal experimental conditions, this PEC biosensor showed a wide linear range of 0.01−200 nM and a low detection limit of 2.7 pM (S/N = 3). Due to the specific covalent reaction between $-NH_2$ and −CHO, the biosensor presented high detection sensitivity, even discriminating 5fC with 5-methylcytosine and 5-hydroxymethylcytosine. The biosensor was then applied to investigate the effect of heavy metal Cd^{2+} on 5fC content in the root, stem, and leaves of maize seedlings.

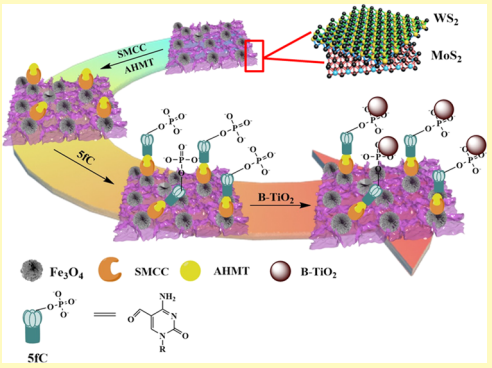

KEYWORDS: *photoelectrochemical biosensor, DNA formylation, MoS_2/WS_2 heterojunction, black TiO_2, eco-toxicological effect, maize seedling*

In recent years, various epigenetic modifications of nucleic acids have attracted extensive attention due to their important roles in cell differentiation, DNA replication, transcription, and translation in organisms.[1] 5-Formylcytosine (5fC), as an important epigenetic modification of cytosine in DNA, plays a unique role in the process of gene regulation.[2] As a derivative produced by further oxidation of 5-hydroxymethylcytosine by ten−eleven translocation (TET) proteins, 5fC is involved in the process of DNA demethylation, regulation of chromatin, cell development, and is even related to the identification of proteins.[3] To understand the biological function of 5fC, accurate detection of 5fC in the genome is necessary. However, due to the low content of 5fC in genomic DNA[4] (less than 1/10 of the 5hmC content), the detection of 5fC is challenging. To date, most detection methods for 5fC have been constructed based on fluorescent labeling, mass spectrometry, and bisulfite-free sequencing methods.[5] Although these techniques have successfully detected 5fC, there are still some disadvantages to be minimized. For example, fluorescent labeling methods are inadequate for the detection of 5fC in samples such as tissues and cells because the obtained limit of detection (LOD) is inappropriate. Similarly, the mass spectrometry method requires harsh reaction conditions, expensive equipment, and skilled operators. Therefore, the development of new detection methods for 5fC detection is necessary.

As an emerging detection technique, photoelectrochemical (PEC) analysis is being actively developed. Hence, PEC analysis has attracted extensive research attention in various fields.[6,7] In the process of PEC detection, a light source is used as the excitation light source and an electrical signal is used as the response signal. The two different forms of light and electricity can be effectively separated, offering the PEC detection method the advantages of both electrochemical and optical methods, including simple operation, fast response, low background signal, inexpensive instrument, and high detection sensitivity.[8] Hence, PEC techniques have been widely applied to bioanalysis, particularly the detection of multiple biomolecules, such as adenosine,[9] microRNA,[10,11] 5-hydroxymethylcytosine,[12] acetylcholinesterase,[13] myoglobin,[14,15] carci-

Received: January 6, 2020
Accepted: March 11, 2020
Published: March 11, 2020

noembryonic antigen,[16] and ATP.[17] Thus, PEC biosensors will provide an ideal platform for 5fC detection.

In general, the photoactive material is a crucial part for constructing the PEC biosensor, which plays a key role in molecular immobilization, signal generation, and signal transmission in the whole system.[18] As a two-dimensional transition-metal dichalcogenide (TMD) with a layered graphene-like structure, molybdenum disulfide (MoS_2) has unique advantages in the applications of sensitive photodetectors,[19] energy storage devices,[20] and light-emitting diodes[21] owing to its layer-controlled band structure and carrier transport properties, which will benefit it as a multifunctional semiconducting optoelectronic material.[22,23] The layer-controlled band structure of MoS_2 makes it have a unique thickness dependence. As the thickness changes, its band gap can changes from an indirect band gap to a direct band gap, showing more excellent physical and chemical properties. At the same time, due to the effects of quantum effects, these layered two-dimensional materials also produce some better characteristics, such as better optical activity. Therefore, it is important to prepare layered molybdenum disulfide nanosheets by micromechanical peeling technology or some other techniques and to effectively regulate the carrier behavior. According to some reports, the bulk MoS_2 can be exfoliated to produce nanosheets by ultrasonic-assisted exfoliation or intercalation method. Because the luminous intensity of MoS_2 is related to its thickness, the exfoliated MoS_2 has strong photoluminescence characteristics and abundant edge active sites, which can greatly improve the photoactivity of MoS_2. However, it still has problems to limit the application of MoS_2 in PEC biosensors, such as low visible light utilization rate, high carrier recombination rate, and low active sites.[24] Therefore, it is necessary to broaden the light absorption range and increase the photoelectric conversion efficiency of MoS_2. One of the effective methods to minimize the rapid recombination of photogenerated electrons and holes in semiconductor materials is to construct a semiconductor heterojunction by combining a narrow band gap semiconductor with pure MoS_2. Because face-to-face contact could provide a maximized interfacial region between the two composites, it largely facilitates charge separation and migration processes.[25,26] In addition, the carriers cross the junction due to the mismatch of electronic structure for both the layers and the barrier heights altered in the process of carrier transport.[27] Therefore, the design of reasonable heterojunction with matched band gaps is believed to be significant in enhancing the photoelectric activity. Tungsten disulfide (WS_2), another well-known layered transition-metal chalcogenide, is particularly attractive due to its narrow band gap (1.2−1.3 eV), large specific surface area, and high carrier mobility.[28] The band edge of the MoS_2 nanosheet matches well with the edge of the WS_2 nanosheet. Therefore, the MoS_2/WS_2 heterojunction can greatly improve the photoactivity of MoS_2. Though this heterojunction has recently received extensive attention and research in many fields,[29−32] a MoS_2/WS_2 heterojunction has rarely been applied as a visible-light-sensitive material in the development of PEC biosensors.

Detection selectivity is another crucial factor for the PEC detection of 5fC. Due to the similar structure to 5-hydroxymethylcytosine (5hmC) and 5-methylationcytosine (5mC),[33] 5fC detection can be greatly influenced by cytosine derivatives. To address this problem, the specific covalent reaction of 5fC can be considered. That is, the only difference between 5fC and other cytosine derivatives is −CHO at its C5 position; thus, 5fC can be specifically discriminated based on the specific covalent chemical reaction of −CHO. Therefore, it is generally necessary to further identify and capture 5fC by introducing an active molecule that can react specifically with the aldehyde group. In general, substances which can react with reactive aldehyde groups include amides, hydroxylamines, hydrazine, ammoniacs, etc.[5,34] It is noteworthy that 4-amino-3-hydrazino-5-mercapto-1,2,4-triazole (AHMT), a well-known Purpald reagent, is often used to detect aldehydes.[35,36] The reaction between hydrazine (on AHMT structure) and the formyl group is highly effective, rapid, and occurs under mild conditions.[37] In addition, the cost of the use of AHMT is low. Due to the above advantages, AHMT was employed as an aldehyde detection reagent.

In this work, a novel, simple, and sensitive PEC biosensor was developed for 5fC detection in the genomic DNA of the roots, stems, and leaves of maize seedlings. A MoS_2/WS_2 heterojunction nanocomposite was employed as a photoactive material, AHMT was used as a linker in the covalent reaction of −CHO, and black TiO_2 (B-TiO_2) was adopted as a signal amplification material. To evaluate the applicability of the biosensor, this PEC biosensor was applied to the investigation of the effect of Cd^{2+} on the 5fC content in roots, stems, and leaves of maize seedlings. In our previous work, the detection of 5fC was performed using PEC techniques.[25,38] However, there are some disadvantages needing to be conquered, including 5fC-contained DNA sequence detection, low detection sensitivity, signal "on−off" model, complicated preparation process of the photoactive material, practical applicability, etc. To dissolve the above questions, the PEC method developed in this work is an "off−on" model using MoS_2, WS_2, and black TiO_2 ternary heterojunction structure, and the detection target is a single 5fC molecule, which can not only improve the detection sensitivity but also expand the applicability of the developed method and even achieve the detection of 5fC content in genomic DNA.

EXPERIMENTAL SECTION

Reagents and Instruments. $FeCl_2{\cdot}4H_2O$, $FeCl_3{\cdot}6H_2O$, (3-aminopropyl) triethoxysilane (APTES), titanium butoxide, ascorbic acid (AA), cadmium nitrate, acetonitrile, and ethanol were received from Aladdin (China). *N*-Succinimidyl 4-(*N*-maleimidomethyl) cyclohexanecarboxylate (SMCC) was provided by Thermo Fisher. MoS_2 powder, WS_2 powder, and white TiO_2 were obtained from Sigma-Aldrich. 4-Amino-3-hydrazino-5-mercapto-1,2,4-triazole (AHMT) was purchased from TCI (JPN). 5-Formyl-2′-deoxycytidine-5′-triphosphate (5f-dCTP), 5-methyl-2′-deoxycytidine-5′-triphosphate (5m-dCTP), and 5-hydroxymethyl-2′-deoxycytidine-5′-triphosphate (5hm-dCTP) were supplied by TriLink Biotechnologies (San Diego). N^1-methyl-2′-adenosine-5′-triphosphate (m^1-ATP) and N^6-methyl-2′-adenosine-5′-triphosphate (m^6-ATP) were purchased from Jena Bioscience (Germany). 2′-Deoxycytidine-5′-triphosphate (dCTP), 2′-deoxyguanosine-5′-triphosphate (dGTP), 2′-deoxyadenosine-5′-triphosphate (dATP), and 2′-deoxythymidine-5′-triphosphate (dTTP) were provided by Sangon (Shanghai, China).

Transmission electron microscopy (TEM) images were obtained on a Tecnai G2 F20 instrument (Fei Company). Scanning electron microscopy (SEM) images were collected on a Quanta Q400. Atomic force microscope (AFM) was performed on a Dimension Icon microscope (Brook) using a tapping mode. Powder X-ray diffractometry (XRD) was performed on a Smartlab SE equipment operated at 40 kV and 30 mA (Toyko, Japan). PEC detection was performed on a CHI832A electrochemical workstation equipped with a 500 W Xe lamp as a light source.[39] A three-electrode system was

https://dx.doi.org/10.1021/acssensors.0c00036
ACS Sens. 2020, 5, 1092−1101

Scheme 1. Schematic Illustration of the Construction Process of the Proposed PEC Biosensor

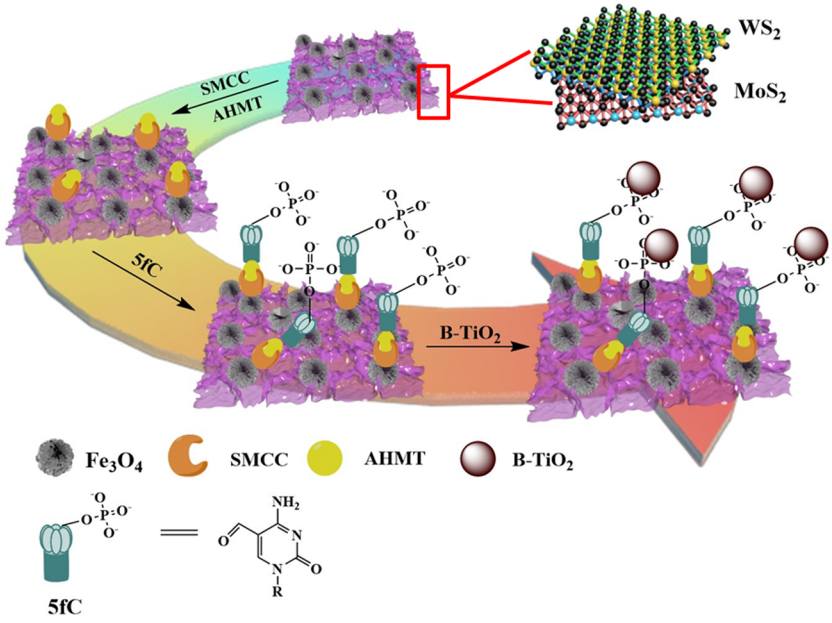

used in the Mott−Schottky experiments, comprising a modified glassy carbon electrode as the working electrode, a Pt wire as the counter electrode, and a standard calomel electrode as the reference electrode.

Synthesis of MoS_2, WS_2 Nanosheets, and Amino-Functionalized Fe_3O_4. MoS_2 nanosheets were prepared using a typical ultrasound method.[40] First, 1 g of MoS_2 powder and 0.3 g of sodium cholate were added into 200 mL of distilled water. Then, the solution was sonicated for 20 h at room temperature. Afterward, the dispersion was centrifuged at 3000 rpm for 15 min to remove any large MoS_2 pieces. Finally, the product was collected by centrifugation (12 000 rpm, 10 min) and washed several times with double-distilled water and ethanol. Finally, it was freeze-dried in vacuum.

WS_2 nanosheets were prepared using the ultrasonic-assisted liquid-phase exfoliation technique as previously reported,[41] where bulk WS_2 powder was employed as a raw material, PAA as an exfoliating reagent, and water as a solvent. Briefly, bulk WS_2 powder (1.5 g) and PAA (420 μL) were added into 20 mL of sterilized water and the mixture was sonicated for 8 h. Then, the dispersion was centrifuged at 3000 rpm for 10 min, and the upper dark green layer was collected, which was further centrifuged at 10 000 rpm for 10 min. The as-obtained black precipitate was washed several times with double-distilled water and finally freeze-dried in vacuum.

Amino-functionalized Fe_3O_4 was prepared by following a previous report, but with some modifications.[42] First, 50 mL of a 0.5 M HCl solution and a known quantity of $FeCl_2{\cdot}4H_2O$ and $FeCl_3{\cdot}6H_2O$ (molar ratio, 1:2) were added into a three-neck flask and stirred under N_2 atmosphere at a 90 °C water bath, followed by the addition of 1.5 M sodium hydroxide solution to adjust the pH to 9.3−9.7. After stirring for 30 min, the prepared Fe_3O_4 was magnetically separated and washed with double-distilled water three times. To modify with amino group, the magnetic particles were first dispersed into 200 mL of ethanol under ultrasonication. Then, 5 mL of 95% APTES was added into the dispersion under N_2 atmosphere and stirred for 2 h at 75 °C. Finally, the prepared amino-functionalized Fe_3O_4 (Fe_3O_4−NH_2) was collected by magnetic separation and the product was washed three times with double-distilled water and ethanol separately. The prepared Fe_3O_4−NH_2 was dried under 60 °C in vacuum.

Synthesis of B-TiO_2 Nanospheres. B-TiO_2 nanospheres were prepared by following a previous report with few modifications.[43] Briefly, 1 g of white TiO_2 and 1 g of $NaBH_4$ were thoroughly ground and transferred to an alumina boat, and calcined at 300 °C for 2 h under a N_2 atmosphere. After being allowed to be at room temperature, the mixture was washed with water and collected by centrifugation. Finally, it was dried at 60 °C before use.

Fabrication of a PEC Biosensor. Before biosensor preparation, three aqueous nanomaterial dispersions (3 mg/mL MoS_2 nanosheets, 2 mg/mL WS_2 nanosheets, and 3 mg/mL NH_2−Fe_3O_4) were ultrasonically prepared.

Indium titanium oxide (ITO) conductive glass pieces were initially cleaned before being used as ITO electrodes, as previously reported by us.[44] After cleaning, 40 μL of the prepared MoS_2, WS_2, and NH_2−Fe_3O_4 dispersion was applied to the ITO surface and dried under an infrared lamp. The obtained electrode was denoted as Fe_3O_4/WS_2/MoS_2/ITO. Then, 40 μL of 1 mg/mL SMCC was applied to the electrode surface and incubated for 2 h under room temperature in a humid cell. The prepared electrode was denoted as SMCC/Fe_3O_4/WS_2/MoS_2/ITO. After that, the electrode was incubated with 20 μL activated propionic acid for 30 min to eliminate the unreacted −NH_2 of NH_2−Fe_3O_4. Subsequently, 40 μL of 100 μg/mL AHMT was placed on the modified electrode surface, which was incubated for 120 min to promote the reaction between SMCC and the sulfydryl group of AHMT. The electrode was denoted as AHMT/SMCC/Fe_3O_4/WS_2/MoS_2/ITO. Afterward, the electrode was further incubated with 40 μL of different concentrations of 5fC for 120 min at 37 °C under humid condition. The obtained electrode was named as 5fC/AHMT/SMCC/Fe_3O_4/WS_2/MoS_2/ITO. Finally, 40 μL of B-TiO_2 was deposited on the electrode surface and incubated for 110 min, producing B-TiO_2/5fC/AHMT/SMCC/Fe_3O_4/WS_2/MoS_2/ITO. It must be emphasized that the electrode was washed three times with washing buffer (10 mM Tris−HCl and 50 mM NaCl, pH 7.4) and dried under a N_2 stream between each modification step.

Sample Preparation and Detection. In this work, the effect of heavy metal Cd^{2+} on 5fC content in maize seedling roots, stems, and leaves was investigated. First, the maize seeds were sterilized in a 2% sodium hypochlorite solution for 5 min and then soaked in distilled water overnight. Next, the full, evenly sized maize seeds were planted on plastic trays exposed to sunlight and moisture every day. During the growth of the seeds into seedlings, different concentrations of Cd^{2+} solution were introduced into the incubation system, and these seedlings were further cultured for 7 days in Petri dishes. Subsequently, the roots, stems, and leaves of these maize seedlings were harvested and immediately frozen in liquid nitrogen before being ground into powder. Afterward, genomic DNA in these maize roots, stems, leaves was extracted using a plant genomic DNA extraction kit (TianGen, Beijing, China). Then, the DNA concentration was

https://dx.doi.org/10.1021/acssensors.0c00036
ACS Sens. 2020, 5, 1092−1101

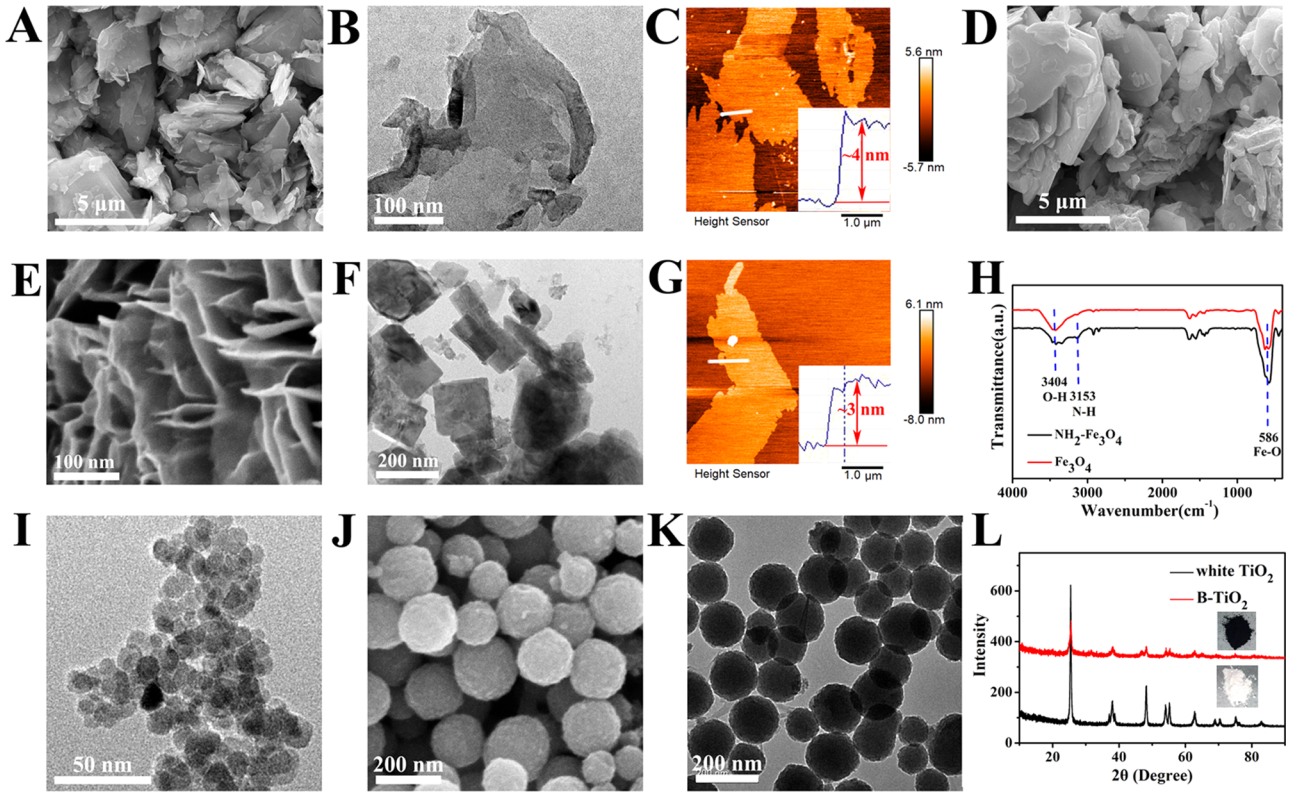

Figure 1. (A) SEM micrograph of bulk MoS_2 powder, (B) TEM micrograph of MoS_2 nanosheets, and (C) AFM micrograph of MoS_2 nanosheets, where the inset is the height profile. (D) SEM micrograph of bulk WS_2 powder, (E) SEM micrograph of WS_2 nanosheets, (F) TEM micrograph of WS_2 nanosheets, and (G) AFM micrograph of WS_2 nanosheets, where the inset is the height profile. (H) FT-IR spectrum of Fe_3O_4 and NH_2−Fe_3O_4, (I) TEM micrograph of Fe_3O_4, (J) SEM micrograph of B-TiO_2, (K) TEM micrograph of B-TiO_2, and (L) XRD pattern of white TiO_2 and B-TiO_2.

measured using a Quawell Q3000 micro-volume UV spectrophotometer (San Jose). Finally, genomic DNA was degraded to its individual nucleotide component by DNA Degradase (Zymo, Japan), which was stored at −80 °C. To detect the 5fC content, the PEC biosensor was fabricated as described in the Experimental Section except that 5fC was replaced by 40 μL of the digested genomic DNA solution.

RESULTS AND DISCUSSION

Detection Strategy. In this work, a novel PEC method was developed to quantitatively detect 5fC. MoS_2/WS_2 heterojunction was employed as a photoactive material. The specific covalent reaction between AHMT and the aldehyde group on 5fC is used to identify and capture 5fC. B-TiO_2 and MoS_2/WS_2 form a ternary heterojunction, and the synergy of the three materials increases the light absorption efficiency and significantly improves the PEC response. The biosensor fabrication process and 5fC detection strategy are illustrated in Scheme 1. First, MoS_2 nanosheets and WS_2 nanosheets were immobilized on the ITO electrode surface to fabricate the WS_2/MoS_2/ITO electrode. Then, Fe_3O_4−NH_2 was further modified on the electrode surface, where Fe_3O_4−NH_2 was employed as the immobilization matrix of SMCC through the specific covalent reaction between SMCC and −NH_2 of Fe_3O_4−NH_2. It is well known that SMCC contains an amine-reactive *N*-hydroxysuccinimide (NHS ester) and a sulfhydryl-reactive maleimide group; thus, it can react with −NH_2 and −SH. Based on the covalent reaction between SMCC and the −SH of AHMT, AHMT was further modified on the electrode surface. Because there is a hydrazine group in the AHMT structure, 5fC was then specifically recognized and captured on the electrode surface through the covalent reaction between the hydrazine group of AHMT and the aldehyde group of 5fC. At this point, the phosphate group of 5fC was oriented away from the electrode surface. Finally, based on the covalent reaction between the phosphate group of 5fC and B-TiO_2, B-TiO_2 was further captured on the electrode surface. The formation of B-TiO_2/WS_2/MoS_2 ternary heterojunction accelerated the transfer of interface electrons, prolonged the lifetime of carriers, and achieved further signal amplification of PEC biosensor. Because the magnitude of the PEC response has a quantitative relationship with 5fC, 5fC can be detected with high sensitivity and selectivity.

Characterization of Materials. The morphologies of MoS_2, WS_2, and B-TiO_2 were first characterized by SEM, TEM, and AFM techniques. The structural properties were studied by powder X-ray diffraction (XRD). Figure 1A presents the scanning electron micrograph of MoS_2 powder that shows a large and block structure with several microns in length. It can be clearly seen from the transmission electron micrograph in Figure S1A that the MoS_2 powder has several layers. Figure 1B,C shows the morphological characteristics of MoS_2 nanosheets. TEM micrograph indicated that MoS_2 possessed a thinner nanosheets structure. The atomic force microscopy (AFM) image of a MoS_2 nanosheet is shown in Figure 1C, and the inset shows a thin thickness estimated as ∼4 nm. According to relevant literature reports, the thickness of a single layer of molybdenum sulfide is 0.8−1 nm.[45] Therefore, it is confirmed that the bulk MoS_2 was successfully exfoliated into a smaller nanosheet with four layers. The

https://dx.doi.org/10.1021/acssensors.0c00036
ACS Sens. 2020, 5, 1092−1101

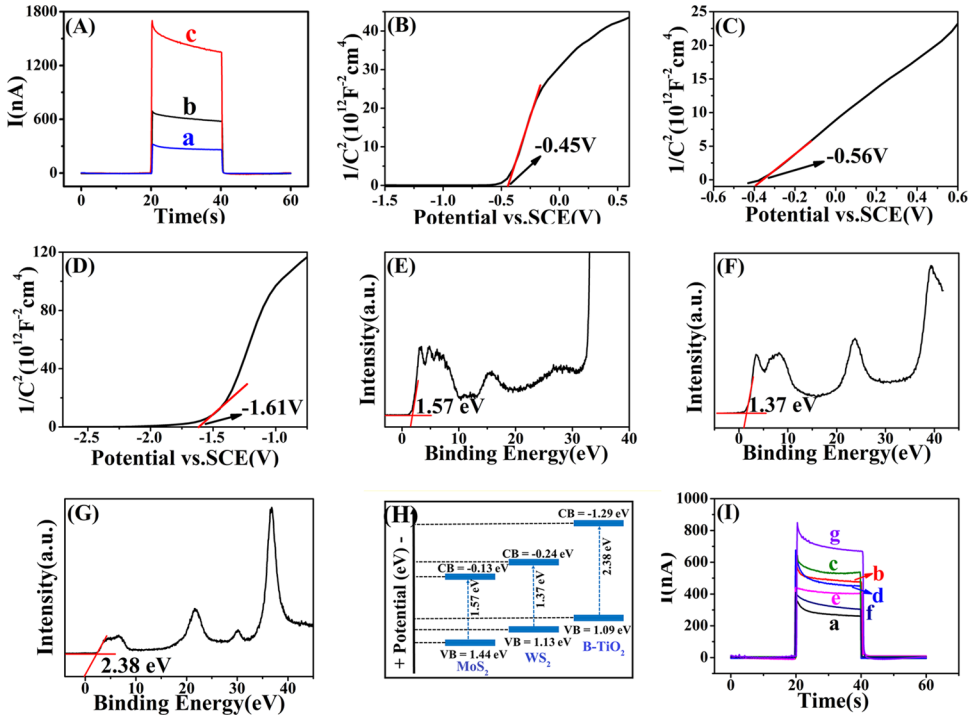

Figure 2. (A) Photocurrent responses of (a) MoS_2/ITO, (b) WS_2/MoS_2/ITO, and (c) B-$TiO_2/WS_2/MoS_2$/ITO in 10 mM Tris−HCl containing 10 mM AA (pH 7.4). (B−D) Mott−Schottky plots of MoS_2, WS_2, and B-TiO_2, respectively. (E−G) VB-XPS spectra of MoS_2, WS_2, and B-TiO_2, respectively. (H) Schematic band structures of MoS_2, WS_2, and B-TiO_2. (I) PEC response of different electrodes in 10 mM Tris−HCl containing 10 mM AA (pH 7.4). (a) MoS_2/ITO, (b) WS_2/MoS_2/ITO, (c) $Fe_3O_4/WS_2/MoS_2$/ITO, (d) SMCC/$Fe_3O_4/WS_2/MoS_2$/ITO, (e) AHMT/SMCC/$Fe_3O_4/WS_2/MoS_2$/ITO, (f) 5fC/AHMT/SMCC/$Fe_3O_4/WS_2/MoS_2$/ITO, and (g) B-TiO_2/5fC/AHMT/SMCC/$Fe_3O_4/WS_2/MoS_2$/ITO. The applied potential is −0.4 V. The 5fC concentration is 1 nM.

scanning electron micrograph of WS_2 powder in Figure 1D indicates a large, block structure similar to that of MoS_2. Moreover, the TEM micrograph (Figure S1B) shows that the WS_2 powder showed a thicker number of layers. The morphology of WS_2 nanosheets was investigated by SEM, which exhibits a relatively thin sheetlike structure (Figure 1E). Figure 1F demonstrates that a WS_2 nanosheet was successfully prepared by the ultrasonic-assisted liquid-phase exfoliation technique. Compared to Figure S1B, not only the thickness is reduced but also the size is significantly reduced, indicating that the large piece of WS_2 was successfully peeled into small nanosheets. The atomic force microscopy (AFM) image of WS_2 nanosheets is shown in Figure 1G, and the inset exhibits a thin thickness estimated as ∼3 nm. According to relevant literature reports, the thickness of a single layer of molybdenum sulfide is 0.8 nm.[46] Therefore, it is confirmed that the bulk WS_2 was successfully exfoliated into smaller nanosheet with four layers. The formed nanoflakes made it a special structure with higher specific surface area. In addition, Fourier transform infrared (FT-IR) spectroscopy was performed to prove the successful preparation of Fe_3O_4 and the successful modification of the amino group. As illustrated in Figure 1H, the stretching vibration of Fe−O (586 cm^{-1}) proves the successful synthesis of Fe_3O_4. After treatment with APTES, the stretching vibration of N−H (3153 cm^{-1}) proved the successful amino functionalization of Fe_3O_4. Fe_3O_4−NH_2 consisted of almost spherical particles with an average size of approximately 10−30 nm (Figure 1I). Interestingly, scanning electron micrograph and transmission electron micrograph of B-TiO_2 showed that B-TiO_2 was spherical in shape with a particle size of 150−200 nm (Figure 1J,K). In addition, B-TiO_2 obtained by the reduction of white TiO_2 is black, which is attributed to the introduction of oxygen vacancies (i.e., Ti^{3+}-V_O sites). The position of the XRD diffraction peaks of white TiO_2 and B-TiO_2 did not change significantly (Figure 1L), proving that both of them have the characteristic of the anatase polymorph of TiO_2. However, after reduction, the XRD peak intensity of B-TiO_2 weakened, which may be the result of the partial loss of crystallinity during the thermal reduction of $NaBH_4$.

To prove the mechanism of PEC signal improvement, some experiments have been carried out, and the energy band structures of MoS_2, WS_2, and B-TiO_2 were analyzed by Mott−Schottky plots[47−49] and valence band photoemission spectrum (VB-XPS)[50−53] in Figure 2. As shown in Figure 2A, the MoS_2/ITO electrode showed an initial photocurrent of about 280 nA (curve a). After WS_2 was coated on the MoS_2/ITO electrode, a larger PEC response of about 597 nA was obtained (curve b). After deposition of B-TiO_2 (curve c), the photocurrent of the B-$TiO_2/WS_2/MoS_2$/ITO electrode greatly increased to 1416 nA. The remarkably increased photocurrent in B-$TiO_2/WS_2/MoS_2$/ITO could be ascribed to faster electron transport from valence band (VB) to conduction band (CB) and a high separation efficiency of the photogenerated electron−hole pairs due to the introduction of B-TiO_2. To further prove it, the band structure of MoS_2, WS_2, and B-TiO_2 was investigated by the Mott−Schottky plots and VB-XPS spectra, which are generally used for the analysis of the flat band potential (E_{fb}) and band gap energy of semiconductor. As shown in Figure 2B−D, the positive slope of the plot indicated that these materials were n-type semiconductors in 0.5 mol/L Na_2SO_4 solution. The E_{fb} values (which were calculated from the

https://dx.doi.org/10.1021/acssensors.0c00036
ACS Sens. 2020, 5, 1092−1101

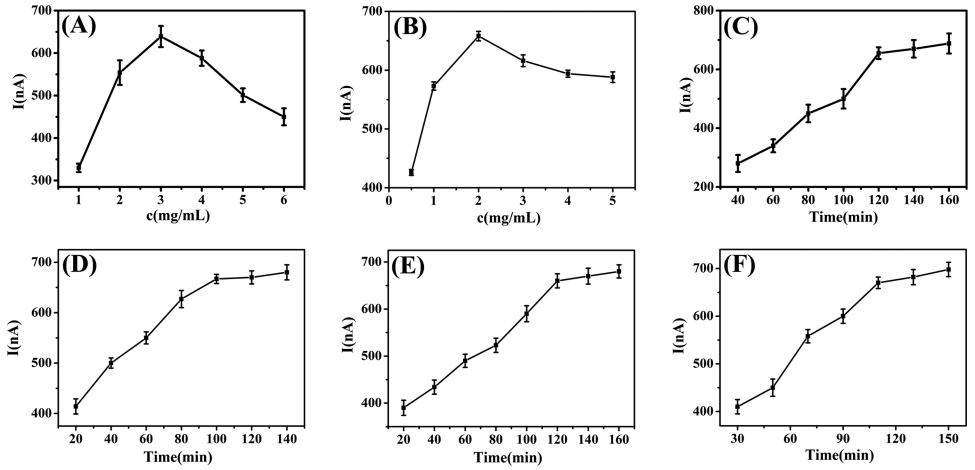

Figure 3. Effects of concentration of MoS_2 (A) and WS_2 (B), incubation time of SMCC (C), AHMT (D), 5fC (E), and B-TiO_2 (F) on PEC response of the biosensor. For (A–F), the 5f-dCTP concentration is 1 nM. The error bar was obtained by three measurements.

intercept of the axis with potential value) were −0.45, −0.56, and −1.61 V vs saturated calomel electrode (SCE) for MoS_2, WS_2, and B-TiO_2, respectively. For many n-type semiconductors, E_{fb} is often estimated to be 0–0.2 V below the conduction band (E_{cb}).[49,54] Based on it, the estimated E_{cb} values of MoS_2, WS_2, and B-TiO_2 were calculated to be −0.13, −0.24, and −1.29 V (vs normal hydrogen electrode (NHE)), respectively,[55−57] or −0.37, −0.48, and −1.53 V (vs SCE), respectively. As seen from Figure 2E–G, the band gap energies (E_g) of MoS_2, WS_2, and B-TiO_2 were estimated to be 1.57, 1.37, and 2.38 eV, respectively. So, the valence band energies (E_{vb}) were 1.44, 1.13, and 1.09 eV, respectively ($E_{vb} = E_{cb} + E_g$). According to these results, the band structures of MoS_2, WS_2, and B-TiO_2 are depicted in Figure 2H. These results prove that the E_{cb} value of B-TiO_2 was higher than those of MoS_2 and WS_2. Thus, the electrons of B-TiO_2 can transfer to WS_2 and further transfer to MoS_2. Moreover, B-TiO_2 can increase the electron transfer amount of WS_2 to MoS_2 due to the energy-level matching of these materials.

Detection Feasibility Assay of the Biosensor. Photocurrent response is an excellent method to characterize the electrode modification process, which can effectively reflect the process of photogenerated electron transfer at different modified interfaces to verify successful modifications. To validate the constructed biosensor, the PEC response of different electrodes was recorded in detection buffer (10 mM Tris–HCl with 10 mM AA, pH 7.4) under visible light illumination.

As shown in Figure 2I, the photocurrent of MoS_2/ITO electrode is about 280 nA (curve a), indicating that MoS_2 nanoflakes have stable and excellent photoelectric activity. After WS_2 was modified on the electrode surface, the photocurrent is significantly increased to 495 nA (curve b). It can be attributed to the formation of a WS_2/MoS_2 heterojunction, where WS_2 can improve the photocurrent response of MoS_2 by accelerating charge separation and retarding electron–hole pair recombination. Because Fe_3O_4 can accelerate the transfer of photogenerated electrons due to its good conductivity, the PEC response increased to 539 nA after Fe_3O_4 was coated on the WS_2/MoS_2/ITO electrode surface (curve c). However, the photocurrent reduced to 475 nA when SMCC was modified on the $Fe_3O_4/WS_2/MoS_2$/ITO electrode (curve d). This is explained by the steric hindrance effect of SMCC, hindering the diffusion of the electron donor (AA) to electrode surface. Subsequently, the photocurrent further decreased to 410 nA when AHMT was immobilized on the electrode surface (curve e), which could be also ascribed to the increased steric hindrance effect. After AHMT/SMCC/$Fe_3O_4/WS_2/MoS_2$/ITO was incubated with 5f-dCTP, the PEC responses decreased to 330 nA (curve f), which could be attributed to the steric hindrance effect and the electrostatic repulsion effect of 5f-dCTP. The transfer of the electron donor to the surface of MoS_2/WS_2 heterojunction is hindered, and as a result, the recombination rate of electrons and holes is increased, thereby reducing the photocurrent. Finally, the photocurrent increased strongly when B-TiO_2 was immobilized on the electrode surface (curve g). It is worth noting that B-TiO_2 formed a ternary heterojunction with MoS_2/WS_2, which accelerated the transfer of electron donors to the electrodes, thereby significantly enhancing photocurrent. According to the change of the PEC response, the successful preparation of the biosensor can be confirmed.

Optimization of PEC Biosensor Testing Conditions. To achieve the high detection sensitivity of the biosensor, several experimental parameters were investigated, including MoS_2 concentration, WS_2 concentration, SMCC incubation time, AHMT incubation time, 5fC incubation time, and B-TiO_2 incubation time. To optimize the experimental conditions, the biosensor was fabricated as described in the Experimental Section except changing the optimal parameter.

As shown in Figure 3A, as MoS_2 concentration increased from 1 to 3 mg/mL, the photocurrent gradually increased to achieve a maximum value at 3 mg/mL. As the concentration of WS_2 continued to increase, the photocurrent gradually decreased. It can be attributed to the increased MoS_2 thickness, which hindered the transfer of electrons to electrode surface, increasing the recombination of photoelectrons and holes. Therefore, 3 mg/mL was chosen as the optimal MoS_2 concentration.

Figure 3B presents the effect of WS_2 concentration. The photocurrent showed a trend of increasing first and then decreasing as the concentration of WS_2 further increased. The PEC signal reached a maximum value with a WS_2 concentration of 2 mg/mL. It can also be ascribed to the increased WS_2 thickness, which hindered the transfer of

https://dx.doi.org/10.1021/acssensors.0c00036
ACS Sens. 2020, 5, 1092−1101

photogenerated electrons. Therefore, 2 mg/mL was employed in this work.

Figure 3C shows the effect of SMCC incubation time on PEC response. With extending the incubation time from 40 to 120 min, the PEC response gradually increased. However, when the incubation time was higher than 120 min, the photocurrent tended to be stable. It may be explained by the fact that the amount of modified amino-functionalized Fe_3O_4 is saturated, and an excessively long incubation time does not further increase the immobilization amount of SMCC, which results in the stabilization of the PEC response. Therefore, 120 min was employed.

The effect of AHMT incubation time is shown in Figure 3D. The photocurrent increased rapidly with extending the AHMT incubation time from 20 to 100 min. When further prolonging the incubation time, the photocurrent gradually reached a steady state. This may be the result of the SMCC saturation reaction and does not further increase the capture of AHMT. Therefore, 120 min was used. Similarly, the effect of 5fC incubation time and B-TiO_2 immobilization time was also investigated. As shown in Figure 3E,F, the optimal experimental conditions were 120 and 110 min, respectively.

Detection Performance. To evaluate the sensitivity of the developed method, the relationship between different concentrations of 5f-dCTP and photocurrent was investigated under optimal experimental conditions. As shown in Figure 4A, as the

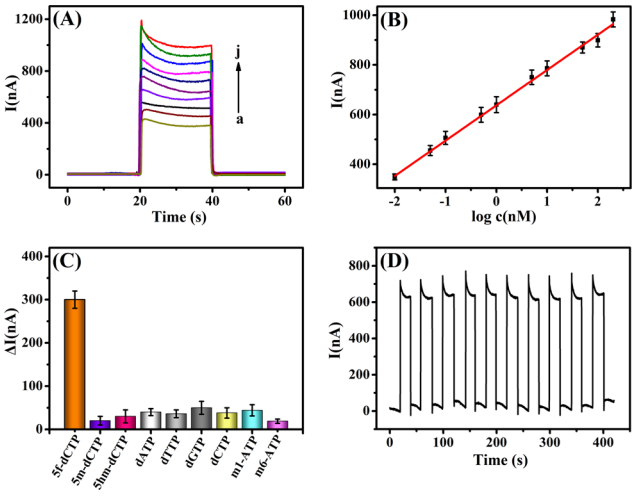

Figure 4. (A) PEC response of the biosensor with various concentrations of 5fC. (a–j) 0.01, 0.05, 0.1, 0.5, 1, 5, 10, 50, 100, 200 nM. (B) Linear relationship between the PEC response and the logarithm value of 5fC concentration. Error bars represent the standard deviation of three measurements. (C) Histogram for the photocurrent change of the biosensor fabricated with different targets. (D) Time-based PEC responses of the biosensor stability test during 10 cycles of light on and light off.

5f-dCTP concentration changes from 0.01 to 200 nM, the photocurrent gradually increased. Within this concentration range, a good linear relationship can be established between the photocurrent and the logarithm value of 5f-dCTP concentration (Figure 4B). The linear regression equation can be expressed as I (nA) = 142 ± 6.77 log c (nM) + 637 ± 9.68 (r = 0.9989, P < 0.0001, n = 10), thus enabling the quantitative detection of 5fC. The detection limit was estimated to be 2.7 pM (S/N = 3). Moreover, we explored the uncertainty (the 95% confidence interval) associated with both the slope and the ordinate intercept of the linear equation. The data are presented in the Supporting Information. These results show that the constructed biosensor has a wide detection range and the detection limit is lower than other methods. In Table 1, the fluorescence detection and

Table 1. Performance Comparison of the PEC Biosensor for 5fC Detection with Other Methods

methods	linear range	detection limit	refs
fluorescence	5–200 nM	10 nM	58
fluorescence	50–1000 nM	42 nM	34
SPME-UPLC-ESI-MS/MS	0.1–100 fM	0.03 fM	59
LC-ESI-MS/MS	0.5–100 fM	0.11 fM	60
photoelectrochemistry	0.01–200 nM	3.8 pM	25
photoelectrochemistry	0.01–200 nM	2.7 pM	this work

analysis technology has the disadvantages of narrow detection range and high detection limit, which limits its use to some extent. Although the liquid chromatography/mass spectrometry detection method significantly expands the detection range and reduces the detection limit, the instrument is not easy to achieve miniaturization and has the disadvantages of expensive and complicated operations. Therefore, the PEC analysis method integrates the advantages of inexpensive instrument, rapid response, and simple operation and thereby becomes a good platform for detecting 5fC. Compared to the previously constructed sensors, this sensor further reduces the detection limit. Thus, the developed method successfully achieves the quantitative monitor of 5fC.

In addition, selectivity and stability play an important role in the performance of biosensor. To investigate the selectivity of the constructed biosensor, eight nucleotides were employed as potential interferents, including 5m-dCTP, 5hm-dCTP, dATP, dTTP, dGTP, dCTP, m1-ATP, and m6-ATP. In the experiment, the biosensor was first prepared with the process as described in the Experimental Section using the above nucleotides and 5f-dCTP. Then, the photocurrent change ($\Delta I = I_2 - I_1$) was compared, where I_2 is the photocurrent of the biosensor fabricated with different nucleotides and I_1 is the biosensor fabricated with 5f-dCTP. As shown in Figure 4C, ΔI for 5f-dCTP was greatly higher than that for other nucleotides, indicating the good detection selectivity of the biosensor. To further prove the detection specificity, the electrode was prepared with the mixture of 5f-dCTP and other eight deoxyribonucleotides, respectively (Figure S2B). The ΔI for 5f-dCTP was similar to the mixture of 5f-dCTP and other deoxyribonucleotides. These results further prove the high detection specificity of the developed method.

SPME-UPLC-ESI-MS/MS: solid-phase microextraction-ultra high-performance liquid chromatography-electrospray ionization-tandem mass spectrometry; LC-ESI-MS/MS: liquid chromatography-electrospray ionization-tandem mass spectrometry.

As another crucial factor, the stability of the PEC biosensor was also investigated by detecting 10 cycles with light on and light off in the detection buffer. As illustrated in Figure 4D, the photocurrent in each cycle showed a small difference with a relative standard deviation (RSD) of 1.48%, indicating acceptable stability.

The reproducibility of the PEC biosensor was assessed with a view toward practical usefulness. To perform it, the photocurrent for eight parallel prepared B-TiO_2/5fC/

https://dx.doi.org/10.1021/acssensors.0c00036
ACS Sens. 2020, 5, 1092–1101

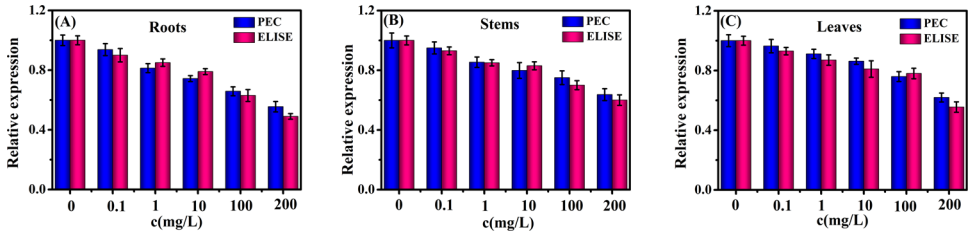

Figure 5. Effect of different concentrations of Cd^{2+} on 5fC content in the genomic DNA of the roots (A), stems (B), and leaves (C) of maize seedling.

AHMT/SMCC/Fe_3O_4/WS_2/MoS_2/ITO electrodes was compared, where the electrodes were fabricated with the same process as described in the Experimental Section. As illustrated in Figure S2C, no significant differences were found in the photocurrent of the eight independent PEC biosensors (RSD 3.71%), indicating acceptable detection reproducibility.

Detection of DNA Formylation in Real-Life Samples. Many factors can influence the growth and yield of crops, such as heavy metals, salt, organic molecule, heat, and chilling.[61−64] Among them, cadmium is a heavy metal most harmful to plant physiological and biochemical processes, mainly in the germination of corn seeds and the elongation of roots, stems, and leaves of crop seedling. Thus, to further evaluate the adaptability of biosensors to 5fC detection and its application prospects, the effects of different concentrations of Cd^{2+} on the 5fC content in the genomic DNA of the roots, stems, and leaves of maize seedlings were investigated. As shown in Figure 5, with increasing Cd^{2+} concentration, the 5fC content gradually decreased in the genomic DNA of roots, stems, and leaves of maize seedlings, which demonstrated that Cd^{2+} can greatly inhibit the expression of 5fC. To verify the accuracy of the method, the expression level of 5fC was also detected by enzyme-linked immunosorbent assay (ELISA), verifying the accuracy of the biosensors. These results also confirmed the great potential of the developed method for detecting 5fC in the genomic DNA of plant tissue.

CONCLUSIONS

In summary, a novel and sensitive PEC biosensor was fabricated for 5fC detection using a MoS_2/WS_2 heterojunction as the photoactive material. With the aid of WS_2, the photoactivity of MoS_2 was improved greatly based on the matched energy band, which can be ascribed to the unique electronic and optical properties of the three different semiconductors and the synergy between the three materials greatly improves the light absorption efficiency, accelerates electron transfer, and extends the lifetime of the carrier. Due to the formation of ternary heterojunction structure between MoS_2, WS_2, and B-TiO_2, the PEC response of the biosensor was further improved by 147.17%, which also increased the detection sensitivity. In our work, AHMT was used as a recognition molecule for 5fC. Based on the specific covalent reaction between the hydrazine structure of AHMT and the −CHO of 5fC, the target molecule was detected with high selectivity. In addition, the proposed biosensor shows great potential for detecting 5fC in the genomic DNA of crop tissues.

ASSOCIATED CONTENT

Supporting Information

The Supporting Information is available free of charge at https://pubs.acs.org/doi/10.1021/acssensors.0c00036.

TEM micrograph of MoS_2 and WS_2 powder (Figure S1); effect of pH on biosensor photocurrent response, PEC response change of the biosensor fabricated with deoxyribonuclestides mixture, and histogram of the photocurrent of the eight biosensors (Figure S2); errors in the slope and intercept of the regression line (Table S1); and 5fC expression in maize roots, stem, and leaves (Tables S2−S4) (PDF)

AUTHOR INFORMATION

Corresponding Author

Huanshun Yin − *College of Chemistry and Material Science, Food Safety Analysis and Test Engineering Technology Research Center of Shandong Province, Shandong Agricultural University, Taian 271018, P. R. China;* orcid.org/0000-0002-5022-0314; Email: yinhs@sdau.edu.cn

Authors

Fei Li − *College of Chemistry and Material Science, Food Safety Analysis and Test Engineering Technology Research Center of Shandong Province, Shandong Agricultural University, Taian 271018, P. R. China*

Siyu Wang − *College of Chemistry and Material Science, Food Safety Analysis and Test Engineering Technology Research Center of Shandong Province, Shandong Agricultural University, Taian 271018, P. R. China*

Yan Chen − *College of Chemistry and Material Science, Food Safety Analysis and Test Engineering Technology Research Center of Shandong Province, Shandong Agricultural University, Taian 271018, P. R. China*

Yunlei Zhou − *College of Chemistry and Material Science, Food Safety Analysis and Test Engineering Technology Research Center of Shandong Province, Shandong Agricultural University, Taian 271018, P. R. China*

Jing Huang − *College of Chemistry and Material Science, Food Safety Analysis and Test Engineering Technology Research Center of Shandong Province, Shandong Agricultural University, Taian 271018, P. R. China*

Shiyun Ai − *College of Chemistry and Material Science, Food Safety Analysis and Test Engineering Technology Research Center of Shandong Province, Shandong Agricultural University, Taian 271018, P. R. China;* orcid.org/0000-0003-0449-3677

Complete contact information is available at: https://pubs.acs.org/10.1021/acssensors.0c00036

https://dx.doi.org/10.1021/acssensors.0c00036
ACS Sens. 2020, 5, 1092−1101

Notes

The authors declare no competing financial interest.

■ ACKNOWLEDGMENTS

This work was supported by the National Key Research and Development Project of China (2018YFC1800605), Key Research and Development Project of Shandong Province of China (2019GSF107023), the National Natural Science Foundation of China (21775090, 41807484, 41977345), and the Natural Science Foundation of Shandong Province of China (ZR2018MB028).

■ REFERENCES

(1) Chen, Y.; Hong, T.; Wang, S.; Mo, J.; Tian, T.; Zhou, X. Epigenetic modification of nucleic acids: from basic studies to medical applications. *Chem. Soc. Rev.* **2017**, *46*, 2844−2872.

(2) Raiber, E.-A.; Portella, G.; Martínez Cuesta, S.; Hardisty, R.; Murat, P.; Li, Z.; Iurlaro, M.; Dean, W.; Spindel, J.; Beraldi, D.; Liu, Z.; Dawson, M. A.; Reik, W.; Balasubramanian, S. 5-Formylcytosine organizes nucleosomes and forms Schiff base interactions with histones in mouse embryonic stem cells. *Nat. Chem.* **2018**, *10*, 1258−1266.

(3) Raiber, E.-A.; Murat, P.; Chirgadze, D. Y.; Beraldi, D.; Luisi, B. F.; Balasubramanian, S. 5-Formylcytosine alters the structure of the DNA double helix. *Nat. Struct. Mol. Biol.* **2015**, *22*, 44−49.

(4) Zhang, H.-Y.; Xiong, J.; Qi, B.-L.; Feng, Y.-Q.; Yuan, B.-F. The existence of 5-hydroxymethylcytosine and 5-formylcytosine in both DNA and RNA in mammals. *Chem. Commun.* **2016**, *52*, 737−740.

(5) Dietzsch, J.; Feineis, D.; Höbartner, C. Chemoselective labeling and site-specific mapping of 5-formylcytosine as a cellular nucleic acid modification. *FEBS Lett.* **2018**, *592*, 2032−2047.

(6) Zhou, Y.; Shi, Y.; Wang, F.-B.; Xia, X.-H. Oriented self-assembled monolayer of Zn(II)-tetraphenylporphyrin on TiO2 electrode for photoelectrochemical analysis. *Anal. Chem.* **2019**, *91*, 2759−2767.

(7) Li, R.; Tu, W.; Wang, H.; Dai, Z. Near-infrared light excited and localized surface plasmon resonance-enhanced photoelectrochemical biosensing platform for cell analysis. *Anal. Chem.* **2018**, *90*, 9403−9409.

(8) Zhao, W.-W.; Xu, J.-J.; Chen, H.-Y. Photoelectrochemical bioanalysis: the state of the art. *Chem. Soc. Rev.* **2015**, *44*, 729−741.

(9) Zhao, Y.; Tan, L.; Gao, X.; Jie, G.; Huang, T. Silver nanoclusters-assisted ion-exchange reaction with CdTe quantum dots for photoelectrochemical detection of adenosine by target-triggering multiple-cycle amplification strategy. *Biosens. Bioelectron.* **2018**, *110*, 239−245.

(10) Wang, H.; Zhang, Q.; Yin, H.; Wang, M.; Jiang, W.; Ai, S. Photoelectrochemical immunosensor for methylated RNA detection based on g-C_3N_4/CdS quantum dots heterojunction and Phos-tag-biotin. *Biosens. Bioelectron.* **2017**, *95*, 124−130.

(11) Hou, T.; Xu, N.; Wang, W.; Ge, L.; Li, F. Truly immobilization-free diffusivity-mediated photoelectrochemical biosensing strategy for facile and highly sensitive microRNA assay. *Anal. Chem.* **2018**, *90*, 9591−9597.

(12) Sui, C.; Li, F.; Wu, H.; Yin, H.; Zhang, S.; Waterhouse, G. I. N.; Wang, J.; Zhu, L.; Ai, S. Photoelectrochemical biosensor for 5hmC detection based on the photocurrent inhibition effect of ZnO on MoS_2/C_3N_4 heterojunction. *Biosens. Bioelectron.* **2019**, *142*, No. 111516.

(13) Hou, T.; Zhang, L.; Sun, X.; Li, F. Biphasic photoelectrochemical sensing strategy based on in situ formation of CdS quantum dots for highly sensitive detection of acetylcholinesterase activity and inhibition. *Biosens. Bioelectron.* **2016**, *75*, 359−364.

(14) Cao, J.-T.; Wang, B.; Dong, Y.-X.; Wang, Q.; Ren, S.-W.; Liu, Y.-M.; Zhao, W.-W. Photogenerated hole-induced chemical redox cycling on $Bi_2S_3/Bi_2Sn_2O_7$ heterojunction: Toward general amplified split-type photoelectrochemical immunoassay. *ACS Sens.* **2018**, *3*, 1087−1092.

(15) Wang, B.; Mei, L.-P.; Ma, Y.; Xu, Y.-T.; Ren, S.-W.; Cao, J.-T.; Liu, Y.-M.; Zhao, W.-W. Photoelectrochemical-chemical-chemical redox cycling for advanced signal amplification: Proof-of-concept toward ultrasensitive photoelectrochemical bioanalysis. *Anal. Chem.* **2018**, *90*, 12347−12351.

(16) Wang, D.; Li, Y.; Lin, Z.; Qiu, B.; Guo, L. Surface-enhanced electrochemiluminescence of Ru@SiO_2 for ultrasensitive detection of carcinoembryonic antigen. *Anal. Chem.* **2015**, *87*, 5966−5972.

(17) Li, M.-J.; Zheng, Y.-N.; Liang, W.-B.; Yuan, R.; Chai, Y.-Q. Using p-type PbS quantum dots to quench photocurrent of fullerene−Au NP@MoS_2 composite structure for ultrasensitive photoelectrochemical detection of ATP. *ACS Appl. Mater. Interfaces* **2017**, *9*, 42111−42120.

(18) Da, H.; Liu, Y.; Li, M.; Yuan, R.; Liu, H.; Chai, Y. A highly sensitive photoelectrochemical $VEGF_{165}$ biosensor with a dual signal amplification strategy by using $AgVO_3$ as a photoactive material. *Chem. Commun.* **2019**, *55*, 8076−8078.

(19) Seo, J.-W. T.; Zhu, J.; Sangwan, V. K.; Secor, E. B.; Wallace, S. G.; Hersam, M. C. Fully inkjet-printed, mechanically flexible MoS_2 nanosheet photodetectors. *ACS Appl. Mater. Interfaces* **2019**, *11*, 5675−5681.

(20) Li, Y.; Chang, K.; Sun, Z.; Shangguan, E.; Tang, H.; Li, B.; Sun, J.; Chang, Z. Selective preparation of 1T- and 2H-phase MoS_2 nanosheets with abundant monolayer structure and their applications in energy storage devices. *ACS Appl. Energy Mater.* **2020**, *3*, 998−1009.

(21) Lopez-Sanchez, O.; Alarcon Llado, E.; Koman, V.; Fontcuberta i Morral, A.; Radenovic, A.; Kis, A. Light generation and harvesting in a van der waals heterostructure. *ACS Nano* **2014**, *8*, 3042−3048.

(22) Jiang, D.; Du, X.; Liu, Q.; Hao, N.; Wang, K. MoS_2/nitrogen doped graphene hydrogels p-n heterojunction: Efficient charge transfer property for highly sensitive and selective photoelectrochemical analysis of chloramphenicol. *Biosens. Bioelectron.* **2019**, *126*, 463−469.

(23) Fang, Y.; Lv, Y.; Gong, F.; Elzatahry, A. A.; Zheng, G.; Zhao, D. Synthesis of 2D-mesoporous-carbon/MoS_2 heterostructures with well-defined interfaces for high-performance lithium-ion batteries. *Adv. Mater.* **2016**, *28*, 9385−9390.

(24) Chou, S. S.; De, M.; Kim, J.; Byun, S.; Dykstra, C.; Yu, J.; Huang, J.; Dravid, V. P. Ligand conjugation of chemically exfoliated MoS_2. *J. Am. Chem. Soc.* **2013**, *135*, 4584−4587.

(25) Li, F.; Yin, H.; Chen, Y.; Wang, S.; Li, J.; Zhang, Y.; Li, C.; Ai, S. Preparation of P-g-C_3N_4-WS_2 nanocomposite and its application in photoelectrochemical detection of 5-formylcytosine. *J. Colloid Interface Sci.* **2020**, *561*, 348−357.

(26) Zou, Y.; Shi, J.-W.; Ma, D.; Fan, Z.; Cheng, L.; Sun, D.; Wang, Z.; Niu, C. WS_2/graphitic carbon nitride heterojunction nanosheets decorated With CdS quantum dots for photocatalytic hydrogen production. *ChemSusChem* **2018**, *11*, 1187−1197.

(27) Li, H.; Yu, K.; Lei, X.; Guo, B.; Fu, H.; Zhu, Z. Hydrothermal synthesis of novel $MoS_2/BiVO_4$ hetero-nanoflowers with enhanced photocatalytic activity and a mechanism investigation. *J. Phys. Chem. C* **2015**, *119*, 22681−22689.

(28) Raza, F.; Park, J. H.; Lee, H.-R.; Kim, H.-I.; Jeon, S.-J.; Kim, J.-H. Visible-light-driven oxidative coupling reactions of amines by photoactive WS_2 nanosheets. *ACS Catal.* **2016**, *6*, 2754−2759.

(29) Chen, K.; Wan, X.; Wen, J.; Xie, W.; Kang, Z.; Zeng, X.; Chen, H.; Xu, J.-B. Electronic properties of MoS_2−WS_2 heterostructures synthesized with two-step lateral epitaxial strategy. *ACS Nano* **2015**, *9*, 9868−9876.

(30) Shi, J.; Tong, R.; Zhou, X.; Gong, Y.; Zhang, Z.; Ji, Q.; Zhang, Y.; Fang, Q.; Gu, L.; Wang, X.; Liu, Z.; Zhang, Y. Temperature-mediated selective growth of MoS_2/WS_2 and WS_2/MoS_2 vertical stacks on Au foils for direct photocatalytic applications. *Adv. Mater.* **2016**, *28*, 10664−10672.

(31) Woods, J. M.; Jung, Y.; Xie, Y.; Liu, W.; Liu, Y.; Wang, H.; Cha, J. J. One-step synthesis of MoS_2/WS_2 layered heterostructures and catalytic activity of defective transition metal dichalcogenide films. *ACS Nano* **2016**, *10*, 2004−2009.

https://dx.doi.org/10.1021/acssensors.0c00036
ACS Sens. 2020, 5, 1092−1101

(32) Pesci, F. M.; Sokolikova, M. S.; Grotta, C.; Sherrell, P. C.; Reale, F.; Sharda, K.; Ni, N.; Palczynski, P.; Mattevi, C. MoS2/WS2 Heterojunction for Photoelectrochemical Water Oxidation. *ACS Catal.* **2017**, *7*, 4990−4998.
(33) Bhutani, N.; Burns, D. M.; Blau, H. M. DNA demethylation dynamics. *Cell* **2011**, *146*, 866−872.
(34) Guo, P.; Yan, S.; Hu, J.; Xing, X.; Wang, C.; Xu, X.; Qiu, X.; Ma, W.; Lu, C.; Weng, X.; Zhou, X. Selective detection of 5-formyl-2′-deoxycytidine in DNA using a fluorogenic hydroxylamine reagent. *Org. Lett.* **2013**, *15*, 3266−3269.
(35) Quesenberry, M. S.; Lee, Y. C. A rapid formaldehyde assay using purpald reagent: Application under periodation conditions. *Anal. Biochem.* **1996**, *234*, 50−55.
(36) Zurek, G.; Karst, U. Microplate photometric determination of aldehydes in disinfectant solutions. *Anal. Chim. Acta* **1997**, *351*, 247−257.
(37) Wang, Y.; Liu, C.; Yang, W.; Zou, G.; Zhang, X.; Wu, F.; Yu, S.; Luo, X.; Zhou, X. Naphthalimide derivatives as multifunctional molecules for detecting 5-formylpyrimidine by both PAGE analysis and dot-blot assays. *Chem. Commun.* **2018**, *54*, 1497−1500.
(38) Li, F.; Zhou, Y.; Wang, S.; Yin, H.; Chen, Y.; Luo, H.; Ai, S. One step preparation of CN-WS_2 nanocomposite with enhanced photoactivity and its application for photoelectrochemical detection of 5-formylcytosine in the genomic DNA of maize seedling. *Biosens. Bioelectron.* **2020**, *151*, No. 111973.
(39) Zhou, Y.; Yin, H.; Sui, C.; Wang, Y.; Ai, S. Photoelectrochemical detection of 5-hydroxymethylcytosine in genomic DNA based on M. *Hha*I methyltransferase catalytic covalent bonding. *Chem. Eng. J.* **2019**, *357*, 94−102.
(40) Li, B. L.; Zou, H. L.; Lu, L.; Yang, Y.; Lei, J. L.; Luo, H. Q.; Li, N. B. Size-dependent optical absorption of layered MoS_2 and DNA oligonucleotides induced dispersion behavior for label-free detection of single-nucleotide polymorphism. *Adv. Funct. Mater.* **2015**, *25*, 3541−3550.
(41) Yuan, Y.; Li, R.; Liu, Z. Establishing water-soluble layered WS_2 nanosheet as a platform for biosensing. *Anal. Chem.* **2014**, *86*, 3610−3615.
(42) Wang, J.; Zheng, S.; Shao, Y.; Liu, J.; Xu, Z.; Zhu, D. Amino-functionalized Fe_3O_4@SiO_2 core−shell magnetic nanomaterial as a novel adsorbent for aqueous heavy metals removal. *J. Colloid Interface Sci.* **2010**, *349*, 293−299.
(43) Wang, M.; Yin, H.; Zhou, Y.; Sui, C.; Wang, Y.; Meng, X.; Waterhouse, G. I. N.; Ai, S. Photoelectrochemical biosensor for microRNA detection based on a MoS_2/g-C_3N_4/black TiO_2 heterojunction with Histostar@AuNPs for signal amplification. *Biosens. Bioelectron.* **2019**, *128*, 137−143.
(44) Wang, M.; Yin, H.; Zhou, Y.; Meng, X.; Waterhouse, G. I. N.; Ai, S. A novel photoelectrochemical biosensor for the sensitive detection of dual microRNAs using molybdenum carbide nanotubes as nanocarriers and energy transfer between CQDs and AuNPs. *Chem. Eng. J.* **2019**, *365*, 351−357.
(45) Yin, W.; Yan, L.; Yu, J.; Tian, G.; Zhou, L.; Zheng, X.; Zhang, X.; Yong, Y.; Li, J.; Gu, Z.; Zhao, Y. High-throughput synthesis of single-layer MoS_2 nanosheets as a near-infrared photothermal-triggered drug delivery for effective cancer therapy. *ACS Nano* **2014**, *8*, 6922−6933.
(46) Xu, Z.-Q.; Zhang, Y.; Lin, S.; Zheng, C.; Zhong, Y. L.; Xia, X.; Li, Z.; Sophia, P. J.; Fuhrer, M. S.; Cheng, Y.-B.; Bao, Q. Synthesis and transfer of large-area monolayer WS_2 crystals: moving toward the recyclable use of sapphire substrates. *ACS Nano* **2015**, *9*, 6178−6187.
(47) Zhang, Y.; Li, Y.; Sun, W.; Yuan, C.; Wang, B.; Zhang, W.; Song, X.-M. Fe_2O_3/BiOI-based photoanode with n-p heterogeneous structure for photoelectric conversion. *Langmuir* **2017**, *33*, 12065−12071.
(48) Xu, Y.; Cheng, C.; Du, S.; Yang, J.; Yu, B.; Luo, J.; Yin, W.; Li, E.; Dong, S.; Ye, P.; Duan, X. Contacts between two- and three-dimensional materials: Ohmic, schottky, and p−n heterojunctions. *ACS Nano* **2016**, *10*, 4895−4919.
(49) Ou, M.; Wan, S.; Zhong, Q.; Zhang, S.; Song, Y.; Guo, L.; Cai, W.; Xu, Y. Hierarchical Z-scheme photocatalyst of g-C_3N_4@Ag/$BiVO_4$ (040) with enhanced visible-light-induced photocatalytic oxidation performance. *Appl. Catal., B* **2018**, *221*, 97−107.
(50) Yang, G.; Chen, D.; Ding, H.; Feng, J.; Zhang, J. Z.; Zhu, Y.; Hamid, S.; Bahnemann, D. W. Well-designed 3D $ZnIn_2S_4$ nanosheets/TiO_2 nanobelts as direct Z-scheme photocatalysts for CO_2 photoreduction into renewable hydrocarbon fuel with high efficiency. *Appl. Catal., B* **2017**, *219*, 611−618.
(51) Guo, Y.; Yang, J.; Chu, S.; Kong, F.; Luo, L.; Wang, Y.; Zou, Z. Theoretical and experimental study on narrowing the band gap of carbon nitride photocatalyst by coupling a wide gap molecule. *Chem. Phys. Lett.* **2012**, *550*, 175−180.
(52) Zhang, X.; Wang, X.; Yi, X.; Ye, J.; Wang, D. Alkali treatment for enhanced photoelectrochemical water oxidation on hematite photoanode. *ACS Sustainable Chem. Eng.* **2019**, *7*, 5420−5429.
(53) Zhu, H.; Chen, Z.; Hu, Y.; Gong, L.; Li, D.; Li, Z. A novel immobilized Z-scheme P3HT/α-Fe_2O_3 photocatalyst array: Study on the excellent photocatalytic performance and photocatalytic mechanism. *J. Hazard. Mater.* **2020**, *389*, No. 122119.
(54) Matsumoto, Y. Energy positions of oxide semiconductors and photocatalysis with iron complex oxides. *J. Solid State Chem.* **1996**, *126*, 227−234.
(55) Tian, H.; Liu, M.; Zheng, W. Constructing 2D graphitic carbon nitride nanosheets/layered MoS_2/graphene ternary nanojunction with enhanced photocatalytic activity. *Appl. Catal., B* **2018**, *225*, 468−476.
(56) Zhang, X.; Wang, J.; Hu, W.; Zhang, K.; Sun, B.; Tian, G.; Jiang, B.; Pan, K.; Zhou, W. Facile strategy to fabricate uniform black TiO_2 nanothorns/graphene/black TiO_2 nanothorns sandwichlike nanosheets for excellent solar-driven photocatalytic performance. *ChemCatChem* **2016**, *8*, 3240−3246.
(57) Zhang, X.; Hu, W.; Zhang, K.; Wang, J.; Sun, B.; Li, H.; Qiao, P.; Wang, L.; Zhou, W. Ti^{3+} self-doped black TiO_2 nanotubes with mesoporous nanosheet architecture as efficient solar-driven hydrogen evolution photocatalysts. *ACS Sustainable Chem. Eng.* **2017**, *5*, 6894−6901.
(58) Xu, L.; Chen, Y.-C.; Chong, J.; Fin, A.; McCoy, L. S.; Xu, J.; Zhang, C.; Wang, D. Pyrene-based quantitative detection of the 5-formylcytosine loci symmetry in the CpG duplex content during TET-dependent demethylation. *Angew. Chem., Int. Ed.* **2014**, *53*, 11223−11227.
(59) Jiang, H.-P.; Liu, T.; Guo, N.; Yu, L.; Yuan, B.-F.; Feng, Y.-Q. Determination of formylated DNA and RNA by chemical labeling combined with mass spectrometry analysis. *Anal. Chim. Acta* **2017**, *981*, 1−10.
(60) Tang, Y.; Zheng, S.-J.; Qi, C.-B.; Feng, Y.-Q.; Yuan, B.-F. Sensitive and simultaneous determination of 5-methylcytosine and its oxidation products in genomic DNA by chemical derivatization coupled with liquid chromatography-tandem mass spectrometry analysis. *Anal. Chem.* **2015**, *87*, 3445−3452.
(61) Song, W. Y.; Peng, S. P.; Shao, C. Y.; Shao, H. B.; Yang, H. C. Ethylene glycol tetra-acetic acid and salicylic acid improve anti-oxidative ability of maize seedling leaves under heavy-metal and polyethylene glycol 6000-simulated drought stress. *Plant Biosyst.* **2014**, *148*, 96−108.
(62) Zhang, M.; Zhang, G.-Q.; Kang, H.-H.; Zhou, S.-M.; Wang, W. TaPUB1, a putative E3 Ligase gene from wheat, enhances salt stress tolerance in transgenic nicotiana benthamiana. *Plant Cell Physiol.* **2017**, *58*, 1673−1688.
(63) Li, J.; Wang, Y.; Yu, B.; Song, Q.; Liu, Y.; Chen, T. H. H.; Li, G.; Yang, X. Ectopic expression of StCBF1and ScCBF1 have different functions in response to freezing and drought stresses in Arabidopsis. *Plant Sci.* **2018**, *270*, 221−233.
(64) Wang, G.; Kong, F.; Zhang, S.; Meng, X.; Wang, Y.; Meng, Q. A tomato chloroplast-targeted DnaJ protein protects Rubisco activity under heat stress. *J. Exp. Bot.* **2015**, *66*, 3027−3040.

https://dx.doi.org/10.1021/acssensors.0c00036
ACS Sens. 2020, 5, 1092−1101